



# KIC 3440495: A Rapidly Rotating $\delta$ Scuti- $\gamma$ Doradus Hybrid Pulsator in a Binary System

Shuguo Ma<sup>1,2</sup> , Ali Esamdin<sup>1,2</sup> , Antonio García Hernández<sup>3</sup>, Simon J. Murphy<sup>4</sup> , Chenglong Lv<sup>1,2</sup> , Peng Wei<sup>1</sup> , Michel Rieutord<sup>5</sup> , Javier Pascual-Granado<sup>6</sup> , Fei Dang<sup>1</sup>, Hubiao Niu<sup>1</sup>, TaoZhi Yang<sup>7</sup> , Guojie Feng<sup>1</sup>, Rivkat Karimov<sup>8</sup>, and Yusuf Tillayev<sup>8</sup>

<sup>1</sup> Xinjiang Astronomical Observatory, Chinese Academy of Sciences, Urumqi, Xinjiang 830011, People's Republic of China; [mashuguo@xao.ac.cn](mailto:mashuguo@xao.ac.cn), [aliyi@xao.ac.cn](mailto:aliyi@xao.ac.cn)

<sup>2</sup> School of Astronomy and Space Science, University of Chinese Academy of Sciences, Beijing 100049, People's Republic of China

<sup>3</sup> Theoretical Physics and the Cosmos, University of Granada, E-18071, Granada, Spain

<sup>4</sup> Centre for Astrophysics, University of Southern Queensland, Toowoomba, QLD 4350, Australia

<sup>5</sup> IRAP, Université de Toulouse, CNRS, UPS, CNES, 14, Avenue Édouard Belin, F-31400 Toulouse, France

<sup>6</sup> Instituto de Astrofísica de Andalucía, Glorieta de la Astronomía s/n, E-18008 Granada, Spain

<sup>7</sup> School of Physics, Xi'an Jiaotong University, Xi'an 710049, People's Republic of China

<sup>8</sup> Ulugh Beg Astronomical Institute, Uzbekistan Academy of Sciences, Tashkent 100052, Uzbekistan

Received 2022 May 28; revised 2022 August 22; accepted 2022 August 22; published 2022 September 30

## Abstract

In this paper, we study the pulsation properties of KIC 3440495 using Kepler and TESS data. A Fourier analysis of the light curve reveals 24 pulsation modes as well as 29 frequencies associated with rotation. The rotation frequency is derived to be  $f_{\text{rot}} = 2.322909(2) \text{ day}^{-1}$ , and the rotational modulation is determined to be caused by starspots. A large frequency separation of  $\Delta\nu = 54.5 \mu\text{Hz}$  is found by using a Fourier transform, the autocorrelation function, a histogram of frequency differences, and an échelle diagram. We use the large separation to estimate the refined stellar parameters of the star to be  $v = [239, 279] \text{ km s}^{-1}$ ,  $M = [1.5, 1.65] M_{\odot}$ ,  $R_{\text{equator}} = [2.03, 2.30] R_{\odot}$ ,  $R_{\text{polar}} = [1.72, 1.78] R_{\odot}$ , and  $\omega = [0.61, 0.77]$ . The phase modulations of the pulsating frequencies show a long-term trend which may be attributed to an orbital effect of a binary system; hence, the star may be a fast rotating pulsator in a binary system. KIC 3440495 has an amplitude spectrum similar to Altair, and is identified as a potential sister of Altair. Based on studies of Altair, KIC 3330495 is presumably a young star at a similar evolutionary stage.

*Unified Astronomy Thesaurus concepts:* [Stellar rotation \(1629\)](#); [Stellar pulsations \(1625\)](#); [Starspots \(1572\)](#)

## 1. Introduction

$\delta$  Scuti (Sct) and  $\gamma$  Doradus (Dor) variables are generally A- to F-type pulsators on or near the main sequence (MS), and occupy overlapping regions in the Hertzsprung–Russell diagram.  $\delta$  Sct stars have intermediate masses between 1.2 and  $2.5 M_{\odot}$ , and  $\gamma$  Dors have masses between 1.3 and  $1.8 M_{\odot}$ .  $\delta$  Sct stars usually pulsate in radial and nonradial low- and intermediate-order pressure ( $p$ ), gravity ( $g$ ), and mixed modes with frequencies between  $3 \text{ day}^{-1}$  and  $80 \text{ day}^{-1}$  (Uytterhoeven et al. 2011; Breger et al. 2012; Sánchez Arias et al. 2018). These pulsations can be driven by the  $\kappa$  mechanism operating in the He II ionization zone (Chevalier 1971; Breger 2000), turbulent pressure acting in the hydrogen ionization zone (Antoci et al. 2014; Xiong et al. 2016), and the edge-bump mechanism (Stellingwerf 1979; Murphy et al. 2020), which depend on the evolutionary stage and history of the  $\delta$  Sct star.  $\gamma$  Dor stars pulsate in gravity ( $g$ ) modes with high radial orders ( $20 \leq n \leq 100$ ) and low degrees ( $l \leq 4$ ) (Li et al. 2020), and these modes are driven by the convective flux blocking mechanism operating in the base of their convective envelopes (Grigahcène et al. 2005; Dupret et al. 2006). Their pulsation frequencies are usually between  $0.3 \text{ day}^{-1}$  and  $3.3 \text{ day}^{-1}$  (Kaye et al. 1999; Li et al. 2020). When a  $\gamma$  Dor star rotates rapidly, its frequencies can reach up to  $7 \text{ day}^{-1}$  (Bouabid et al. 2013; Ouazzani et al. 2017). In the overlapping instability strip of  $\delta$  Scts and  $\gamma$  Dors stars, so-called “hybrid” pulsators showing

both  $p$ - and  $g$ -mode pulsations have been discovered in abundance in the last decade (Grigahcène et al. 2010; Balona 2018). These hybrid pulsators seem to narrow the distinction between  $\delta$  Sct stars and  $\gamma$  Dor stars. Moreover, they are particularly suitable targets for asteroseismology, since the simultaneous presence of different types of pulsation modes suggests that different driving mechanisms can coexist in a pulsating variable star, providing additional constraints for theoretical models, and allow probing different regions of the stellar interior (Bouabid et al. 2009; Kurtz et al. 2014; Saio et al. 2015; Xiong et al. 2016). However, hybrid pulsators generally have messy amplitude spectra, which complicates the mode identification.

Intermediate-mass pulsators ( $\delta$  Sct,  $\gamma$  Dor, hybrid pulsator, etc.) are usually moderate-to-fast rotators (Suárez et al. 2005; Royer et al. 2007; Zorec & Royer 2012). In the rapidly rotating regime, these pulsators may exhibit  $r$  modes (global Rossby waves) (Van Reeth et al. 2016; Saio et al. 2018b; Li et al. 2019). The  $r$  modes are inertial modes, different from the  $g$  and  $p$  modes of asteroseismology. The global toroidal motions get coupled with the spheroidal motion caused by the Coriolis force, which results in temperature perturbations and makes  $r$  modes visible (Berthomieu & Provost 1983; Saio et al. 2018a). These  $r$  modes usually appear at frequencies close to the rotational frequency and its harmonics (Saio et al. 2018b; Samadi-Ghadim et al. 2020). In addition, fast rotation breaks the degeneracy of frequency patterns in the azimuthal order and introduces additional patterns in the spectrum, called rotational splitting (Goupil et al. 2005). When a rotation velocity exceeds  $100\text{--}200 \text{ km s}^{-1}$ , the star is no longer spherically symmetric but oblate due to the centrifugal force. The change in stellar

structure causes a change in the propagation cavity of the modes, which breaks the characteristic pattern of symmetric multiplets split by rotation (Lignières et al. 2006). The asymmetrical multiplets further challenge the identification of the pulsating modes.

The NASA space mission Kepler was launched in 2009 March, and represents a very good opportunity for investigating many kinds of variable stars (Koch et al. 2010). With photometric precision on the order of a few parts per million in flux and continuous collection for about a four year time span, Kepler data are ideally suited for asteroseismology (Gilliland et al. 2010). The large number of observations from Kepler has provided excellent samples for studying the pulsational behaviors of each pulsation class. The Transiting Exoplanet Survey Satellite (TESS) was launched in 2018 to search the entire sky for both astrophysical variability and transiting exoplanets (Ricker et al. 2015). TESS data have a precision of up to a few hundred parts per million in flux, and can identify flux variability on timescales of minutes to weeks. Due to the wide sky coverage and almost continuous photometry, TESS data are making remarkable contributions to the study of stellar pulsations (Stello et al. 2022; Barac et al. 2022; Molnár et al. 2022).

KIC 3440495 is a target observed by the Kepler and TESS missions, and is classified as a  $\delta$  Sct in the Kepler Input Catalog (KIC). The light curve of the Kepler short-cadence data of KIC 3440495 displays a period modulation (Figure 1), and its amplitude spectrum shows frequencies at low and high frequencies (Figure 2). Moreover, Uytterhoeven et al. (2011) analysed the star with the Kepler data and found eight independent frequencies in a range 4.1–21.7 day<sup>-1</sup>, but a detailed frequency analysis has not yet been done. Nielsen et al. (2013) examined the periodic variation of the light curve of the star by using a Lomb–Scargle periodogram and came up with a rotation period of 1.6(3) days. Therefore, the star may be a hybrid pulsator with rotational modulation, which drew our attention. Murphy et al. (2018) used pulsational phase modulation to discover that the star may be in a binary system. Stassun et al. (2019) estimated some parameters of KIC 3440495 based on astrometric and photometric measurements from the Gaia Mission (Stassun et al. 2019). The effective temperature ( $T_{\text{eff}}$ ) of KIC 3440495 is estimated to be 7596(140) K from the photometric measurements. Its radius is estimated to be 1.84(6)  $R_{\odot}$  by using the Gaia parallaxes and  $T_{\text{eff}}$ . Assuming the star is on the MS, or not too far evolved from the MS, the star’s mass is estimated to be 1.8(3)  $M_{\odot}$  from the  $T_{\text{eff}}$ –mass relation. These parameters of the star are adopted in the TESS Input Catalog (TIC). Moreover, there are two available low-resolution LAMOST spectra of KIC 3440495. The signal-to-noise ratio (S/N) of the first spectrum is about 591, and that of the second is about 27. Using the first spectrum, Xiang et al. (2022) derived a  $T_{\text{eff}}$  of 7271(82) K, a [Fe/H] of  $-0.2(1)$  dex, a  $\log g$  of 3.9(2) dex, a projected rotation velocity ( $v \sin i$ ) of 239(27) km s<sup>-1</sup>, and a line-of-sight velocity ( $RV$ ) of  $-24.7(4)$  km s<sup>-1</sup> for the star. With the empirical relations between  $\log M$  (mass),  $\log R$  (radius), and  $T_{\text{eff}} + \log g + [\text{Fe}/\text{H}]$  (Moya et al. 2018; Moya & López-Sastre 2022), we estimate the mass and radius of the star at 1.7(2)  $M_{\odot}$  and 2.4(7)  $R_{\odot}$  using these parameters obtained from the first spectrum. The values in parentheses are the errors of the measurements. These parameters of the star are displayed in Table 1.

The paper is laid out as follows: in Section 2, we introduce the observations and data reduction of KIC 3440495; in Section 3, the detailed analysis of the frequency properties are presented. Some discussions on the properties of KIC 3440495 are made in Section 4, and we present a summary in Section 5.

## 2. Observations and Data Reduction

KIC 3440495 was observed by Kepler in two kinds of collection modes: short cadence (KSC) with a sampling time of 58.9 s and long cadence (KLC) with a sampling time of 29.4 minutes. We downloaded all the Kepler light curves from the Mikulski Archive for Space Telescopes (MAST) server. Processed with the NASA Kepler Data Processing Pipeline (Stumpe et al. 2014), all the Kepler data contain simple aperture photometry (SAP) fluxes and Pre-search Data Conditioning Simple Aperture Photometry (PDC\_SAP) fluxes. Most of the discontinuities, outliers, systematic trends, and other instrumental signatures contained in the SAP fluxes have been removed from the PDC\_SAP fluxes. In the PDC\_SAP flux data of KIC 3440495, the KSC data contain 43,073 points covering a time span of 30.3 days, and the KLC data contain 65,244 points covering a time span of 1470.5 days. We used the PDC\_SAP fluxes for the frequency analysis of KIC 3440495.

KIC 3440495 is also observed in Sectors 14, 40, and 41 of the TESS mission. The data in Sector 14 (S14) are long cadence (TLC) with a sampling time of 1425.6 s, and the data in Sectors 40 (S40) and 41 (S41) are short cadence (TSC) with a sampling time of 475.2 s. The light-curve file of the long-cadence data in S14 can be downloaded from MAST (Jenkins et al. 2016). In S40 and S41, only the target pixel files (TPFs) which contain images for each observation are available on the MAST archive. We downloaded these TPFs and processed the data using basic aperture photometry. The SAP fluxes of KIC 3440495 were extracted from the TPFs of S40 and S41. Details of the aperture photometry are described in Appendix A.

The light curves of the SAP fluxes in S40 and S41 have no obvious systematic trends. Without further corrections done, the SAP fluxes are used for the frequency analysis. The two light-curve files in S40 and S41 are combined to one light curve because of the same exposure time and the almost continuous time span. In the TESS data, the data set of S14 contains 757 points covering a time span of 26.8 days, and the whole data set of S40 and S41 contains 7475 points covering a time span of 55.9 days. The detailed time spans of the Kepler and TESS data are given in Table 2.

We used the normalized fluxes for the subsequent analysis of KIC 3440495, in units of intensity (ppm). The corrected light curves constructed from the Kepler and TESS short- and long-cadence data are shown in Figure 1.

The PYTHON package *Lightkurve* is a useful tool to analyse archive data Kepler and TESS data (Lightkurve Collaboration et al. 2018). We used the package to access, check, and combine multiple quarters of data from MAST. The *Lightkurve* package is also used to remove outliers and to detrend and normalize the light curve. In addition, the aperture photometry for TPFs is done with the *Lightkurve* package.

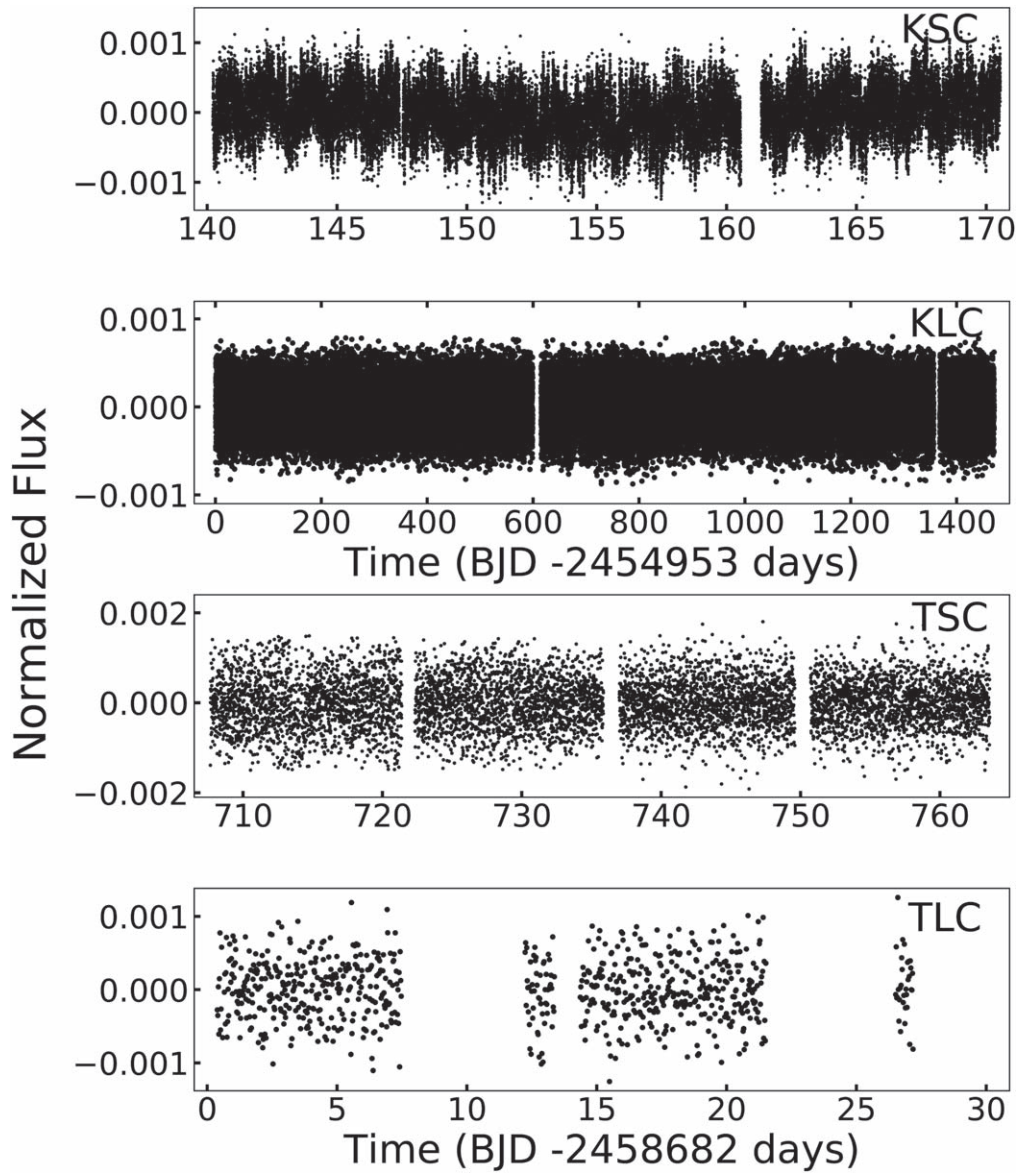


**Figure 1.** The light curves of KIC 3440495 made from the Kepler and TESS short- and long-cadence data. Note the difference of y-axis scales in the panels.

### 3. Frequency Analysis

In order to analyse the pulsation content, we use a discrete Fourier transform (FT) to calculate the amplitude spectra of the Kepler and TESS data (Kurtz 1985). The amplitude spectra are in the range of zero to the Nyquist frequency. The Nyquist frequency,  $f_{\text{Nyq}} = 1/(2 \Delta t)$ , where  $\Delta t$  is the time interval of a discrete data set, is the highest frequency that is not undersampled for a given sampling frequency. The Nyquist frequencies have values of  $24.47 \text{ day}^{-1}$  and  $694.06 \text{ day}^{-1}$  for the KLC and KSC data, and  $23.99 \text{ day}^{-1}$  and  $71.99 \text{ day}^{-1}$  for the TLC and TSC, respectively. The peaks in the amplitude spectra were extracted with the software PERIOD04 (Lenz & Breger 2005), using a multifrequency nonlinear least-squares fit to calculate and optimize the frequency parameters with the following equation:

$$\Delta L = \sum_{i=1}^N A_i \sin(2\pi(f_i t + \phi_i)), \quad (1)$$

where  $A_i$ ,  $f_i$ , and  $\phi_i$  are the amplitude, frequency, and phase of each peak, respectively. We constructed a light curve by using the solution of the frequency in Equation (1), and subtracted this light curve from the data. The residual data were used as input for the next iteration. We performed multiple iterations of prewhitening the data until there were no significant frequencies in the amplitude spectrum. The criterion for judging significant peaks is a S/N greater than or equal to 5, as suggested by Baran et al. (2015). The S/N was calculated in a bin of  $2 \text{ day}^{-1}$  centered on the extracted frequency. The uncertainties on the frequencies and their amplitudes and phases were calculated with Monte Carlo simulations (Montgomery & O’Donoghue 1999).

Two or several close peaks are resolved if their frequency difference is greater than the resolution frequency,  $f_{\text{res}} = 1.5/T$ , where  $T$  is the time span of each data set. The resolution frequencies are values of  $0.001020 \text{ day}^{-1}$  and  $0.04950 \text{ day}^{-1}$  for the KLC and KSC data, and  $0.056 \text{ day}^{-1}$  and  $0.0268 \text{ day}^{-1}$  for the TLC and TSC data, respectively. The KLC data

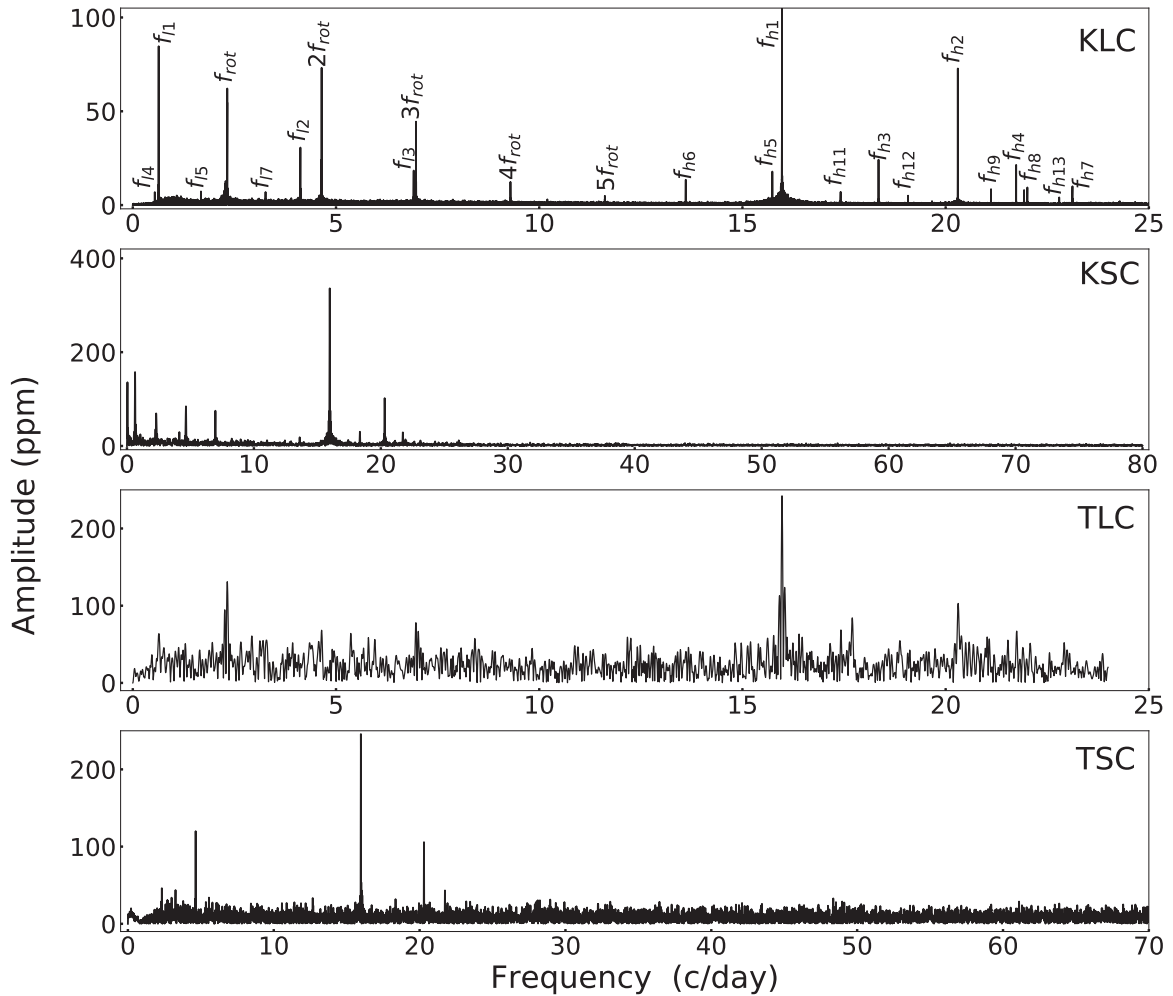


Figure 2. The amplitude spectra of KIC 3440495 from the Kepler and TESS data.

Table 1  
Parameters of KIC 3440495

Parameters	Values	References
Kepler ID	3440495	
TIC ID	122450727	
R.A.(J2000)	+19 <sup>h</sup> :22 <sup>m</sup> :12 <sup>s</sup> .4	
Decl.(J2000)	+38°:30':32".6	
Kmag	10.5 mag	(a)
Contamination	0.004	(a)
log <i>g</i>	4.15(8) dex	(b)
	3.9(2) dex	(c)
<i>T</i> <sub>eff</sub>	7596(140) K	(b)
	7271(82) K	(c)
[Fe/H]	-0.2(1) dex	(c)
<i>v</i> sin <i>i</i>	239(27) km s <sup>-1</sup>	(c)
<i>RV</i>	-24.7(4) km s <sup>-1</sup>	(c)
<i>M</i>	1.8(3) <i>M</i> <sub>⊙</sub>	(b)
	1.7(2) <i>M</i> <sub>⊙</sub>	
<i>R</i>	1.84(6) <i>R</i> <sub>⊙</sub>	(b)
	2.4(7) <i>R</i> <sub>⊙</sub>	
<i>L</i>	10.2(5) <i>L</i> <sub>⊙</sub>	(b)
Distance	412(4) pc	(b)

Note. (a) KIC (Kepler Mission Team 2009). (b) TIC (Stassun et al. 2019). (c) Xiang et al. (2022).

therefore have the best frequency resolution and afford the greatest precision. In what follows, we will primarily use the KLC data set. We first used the KSC data to check for Nyquist aliases (Murphy 2012); these data reveal that all of the real frequencies lie below the KLC Nyquist frequency of 24.49 day<sup>-1</sup>. We present all the amplitude spectra of the Kepler and TESS data in Figure 2.

It can be seen that the significant frequencies in the KLC amplitude spectrum are concentrated in the low- and high-frequency regions. The significant frequencies in the low-frequency region include pulsation frequencies, as well as frequencies related to modulation. The maximum peak in the low-frequency region is at 11.61573 day<sup>-1</sup>, which is the harmonic frequency of the modulation frequency. The minimum peak in the high-frequency region is at 13.60572 day<sup>-1</sup>. Therefore, the boundary between the low- and high-frequency regions in the KLC amplitude spectrum is set at 12 day<sup>-1</sup>. Based on the distribution characteristics of the frequencies in the amplitude spectrum, we divide the frequencies of the KLC data into three parts: high frequencies (marked as  $f_{hi}$ ,  $f_{hi} \geq 12$  day<sup>-1</sup>), low frequencies (marked as  $f_{li}$ ,  $f_{li} \leq 12$  day<sup>-1</sup>), frequencies related to the modulation (marked as  $f_{mi}$ ). This classification is only to facilitate the subsequent discussion and does not address the identification of pulsation patterns. The three groups of the frequencies are numbered in order of S/N

**Table 2**  
The Observation Times of the Kepler and TESS Data of KIC 3440495

Mission	Cadence	Exptime (s)	Start Time (BJD)	End Time (BJD)	Time Span (days)
Kepler	Q3.1	58.9	2455093.2(2009.09.19)	2455123.5(2009.10.19)	30.3
Kepler	Q0-Q17	1800	2454953.0(2009.05.02)	2456423.5(2013.05.11)	1470.5
TESS	Sector 14	1425.6	2458682.9(2019.07.18)	2458709.7(2019.08.14)	26.8
TESS	Sector 40	475.2	2459390.2(2021.06.25)	2459418.4(2021.07.23)	28.2
TESS	Sector 41	475.2	2459419.5(2021.07.24)	2459446.1(2021.08.20)	26.6

from highest to lowest, respectively. All the frequencies extracted from the KLC data are listed in Table 3, and some significant frequencies are tagged in the KLC spectrum of Figure 2. Frequencies extracted from other data sets are also reported in Appendix B, and their serial numbers in the other data sets are kept in line with the frequencies in the KLC data. The errors of these frequencies and their amplitudes are given in parentheses.

### 3.1. The Frequencies in The KLC Spectrum

We detected 53 significant peaks in the amplitude spectrum constructed from the KLC data (Table 3). The significant peaks appear at both low and high frequencies: 36 significant peaks in the range 0.3–12 day<sup>-1</sup> and 17 significant peaks in the range 12–25 day<sup>-1</sup>. The two dominant peaks in the high-frequency region are  $f_{h1} = 15.973311(7)$  day<sup>-1</sup> with an amplitude of  $A_1 = 272(1)$  ppm, and  $f_{h2} = 20.299433(7)$  day<sup>-1</sup> with an amplitude of  $A_2 = 73(1)$  ppm. The two frequencies have a period ratio of 0.786885, which is close to the expected period ratio of the fundamental and first overtone radial pulsations (Stellingwerf 1979). They are probably radial pulsations.

The 36 significant peaks in the range 0.3–12 can be divided into two types: pulsations and frequencies associated with the modulation. The dominant frequency ( $f_{l1}$ ) in the low-frequency region is at 0.636467 day<sup>-1</sup>. Nielsen et al. (2013) automated the analysis of the amplitude spectrum constructed with the eight consecutive Kepler quarters (Q2–Q9), attributing the strongest peak in the frequency range 0.03–1 day<sup>-1</sup> as the rotation frequency. So the frequency  $f_{l1}$  was determined as the rotation frequency for the star (Nielsen et al. 2013). As a statistical study, the method used by Nielsen et al. (2013) to determine the rotation frequencies for a number of active stars may be intuitive and plausible. However, the rotation frequency of many fast rotating A/F-type stars is above 1 day<sup>-1</sup> (Zorec & Royer 2012). In addition, it is also common for a g-mode frequency to appear as the dominant frequency at low frequencies (Balona 2014), though relatively few  $\gamma$  Dor stars with regular patterns in their amplitude spectra exhibit peaks as low as  $f_{l1}$  (Li et al. 2020). It is therefore difficult to determine whether  $f_{l1}$  is the rotation frequency without considering other evidence.

The modulation frequency ( $f_{m2}$ ) and its four harmonics ( $f_{m1}$ ,  $f_{m3}$ ,  $f_{m9}$ ,  $f_{m10}$ ) are detected at low frequencies in the KLC data. This peak has a series of harmonics ( $f_{m1}$ ,  $f_{m3}$ ,  $f_{m9}$ ,  $f_{m10}$ ), which suggest that the light variations are non-sinusoidal. Fourier series such as these have been attributed to rotation in the literature (Balona et al. 2015), but a firm theoretical basis is still pending. Therefore, the peak  $f_{m2}$  is a candidate for rotation. The consequences of this identification are discussed in Section 4.2. The possible rotation frequency has a lower S/N than its first harmonic  $f_{m1}$ , and the half of  $f_{m1}$  may be estimated as a more accurate rotation frequency. Therefore, the rotation frequency  $f_{\text{rot}}$  can be 2.322909(2) day<sup>-1</sup> ( $P_{\text{rot}} = 0.430495(1)$  day).

Besides the frequency  $f_{l1}$ , another dominant frequency ( $f_i$ ) at low frequencies is detected at 0.0379 day<sup>-1</sup> in the KSC data. The frequency  $f_i$  corresponds to one modulation with a period of about 26 days for the light curve made from the KSC data, which can be seen in the top panel of Figure 1. The frequency  $f_i$  is detected only in the KSC data, and its authenticity cannot be determined based on the 30.3 day Kepler short-cadence observations. Since this peak is not present in the KLC data, it is probably an artifact. Considering the resolution frequency of KSC, the frequency  $f_{l1}$  is the same as an artifact of the known Kepler’s artifacts,  $f_{\text{downlink}} = 0.031$  day<sup>-1</sup> (Yang et al. 2018). The data downlink process produces a break lasting 24 hr every 32 days, which leads to the artifact  $f_{\text{downlink}}$ . There is a data gap of approximately 24 hr in the KSC data that can be seen in the top panel of Figure 1. Therefore, we speculate that the appearance of  $f_{l1}$  in the KSC spectrum can be attributed to the failure of the de-trending operation of the PDC\_SAP fluxes in the KSC observations.

There are many side peaks around the rotational frequency and its four harmonics. It is no surprise because intrinsically the power spectrum is dense around the frequencies of gravito-inertial modes or pure inertial modes (Dintrans & Rieutord 2000; Rieutord & Valdetarro 2018). By using frequency separations larger than  $f_{\text{res}} = 0.001020$  day<sup>-1</sup> and a S/N higher than 5, 24 side peaks are retained and listed in Table 3.

Fewer frequencies are detected in the TSC and TLC data. The two dominant peaks ( $f_{h1}$ ,  $f_{h2}$ ) at high frequencies and the modulation frequencies associated with rotation are also detected in the TESS data. These frequencies are consistent with those of Kepler within the allowed error range, and are reported in Appendix B. The presence of the rotation frequency in the amplitude spectra of the Kepler and TESS data suggests that the source of the variability should be constant over a long time span (i.e., rotation), even if the manifestation is intermittent or variable (spots).

## 4. Discussion

### 4.1. A $\delta$ Sct– $\gamma$ Dor Hybrid Pulsator in A Binary System

A pulsator in a binary system would exhibit pulsational phase variations caused by the orbital motion. The pulsational phase variations of KIC 3440495 have been found by Murphy et al. (2018), which suggest that the star is in a binary system with a period longer than the time span of the KLC data. We analysed the pulsational phase modulations of the star in detail to obtain more information about the binary system. The light curve made from the KLC data is divided in multiple 10 day segments. These segments are used to calculate the phase shifts of the pulsations, which are converted into light arrival-time delays (Murphy et al. 2014, 2016; Murphy & Shibahashi 2015; Hey et al. 2020, 2022). The four high frequencies with amplitudes greater than 20 ppm in the KLC spectrum are chosen to measure their phase shifts in each segment, and they

**Table 3**  
Frequencies Extracted from the KLC Spectrum

$f_i$	Frequency (day <sup>-1</sup> )	Amplitude (ppm)	S/N	Comment
$f_{h1}$	15.973311(7)	272(1)	678.0	$f_{p1}$
$f_{h2}$	20.299433(7)	73(1)	200.0	$f_{p2}$
$f_{h3}$	18.34848(2)	24(1)	63.7	...
$f_{h4}$	21.73459(2)	23(1)	62.7	...
$f_{h5}$	15.73522(3)	16(1)	39.9	...
$f_{h6}$	13.60572(4)	13(1)	29.4	...
$f_{h7}$	23.12028(5)	10(1)	28.8	...
$f_{h8}$	22.01080(6)	9(1)	24.9	...
$f_{h9}$	21.11618(6)	9(1)	23.6	...
$f_{h10}$	21.92966(7)	8(1)	21.8	...
$f_{h11}$	17.41632(8)	7(1)	18.5	...
$f_{h12}$	19.0752(1)	5(1)	14.0	...
$f_{h13}$	22.7940(2)	4(1)	11.0	...
$f_{h14}$	15.9752(1)	2(2)	5.9	...
$f_{h15}$	22.797(1)	2(2)	5.8	...
$f_{h16}$	24.283(2)	2(1)	5.8	...
$f_{h17}$	22.791(5)	2(2)	5.7	...
$f_{l1}$	0.636467(6)	85(2)	101.4	...
$f_{l2}$	4.12367(2)	31(1)	29.1	...
$f_{l3}$	6.91147(5)	11(1)	12.2	...
$f_{l4}$	0.54088(7)	8(1)	9.2	...
$f_{l5}$	1.67624(7)	7(1)	5.8	...
$f_{l6}$	1.0819(1)	6(2)	5.5	$2f_{l4}$
$f_{l7}$	3.26635(9)	6(1)	5.3	...
$f_{m1}$	4.645818(2)	80(1)	77.9	$2f_{rot}$
$f_{m2}$	2.323181(8)	68(1)	58.2	$f_{rot}$
$f_{m3}$	6.96832(2)	38(1)	44.1	$3f_{rot}$
$f_{m4}$	2.32570(2)	35(1)	30.4	...
$f_{m5}$	2.25426(2)	33(1)	28.0	...
$f_{m6}$	4.64725(2)	27(1)	26.6	...
$f_{m7}$	2.32002(2)	30(1)	25.6	...
$f_{m8}$	2.28370(2)	29(1)	24.8	...
$f_{m9}$	9.29181(4)	14(1)	19.9	$4f_{rot}$
$f_{m10}$	11.61573(4)	9(2)	15.7	$5f_{rot}$
$f_{m11}$	9.29639(5)	8(1)	11.3	...
$f_{m12}$	2.27983(4)	13(1)	11.2	...
$f_{m13}$	2.26385(4)	13(1)	10.8	...
$f_{m14}$	6.96648(7)	9(1)	10.3	...
$f_{m15}$	2.29649(5)	11(1)	9.1	...
$f_{m16}$	2.29125(4)	10(1)	8.8	...
$f_{m17}$	2.28690(5)	10(1)	8.5	...
$f_{m18}$	6.96278(8)	7(1)	8.2	...
$f_{m19}$	4.67955(7)	8(1)	8.0	...
$f_{m20}$	2.26194(6)	9(1)	7.7	...
$f_{m21}$	2.27503(6)	9(1)	7.4	...
$f_{m22}$	2.31805(6)	8(1)	7.2	...
$f_{m23}$	4.64045(8)	7(1)	7.0	...
$f_{m24}$	2.26942(8)	8(1)	7.0	...
$f_{m25}$	2.26633(9)	7(1)	5.8	...
$f_{m26}$	2.24603(8)	7(1)	5.7	...
$f_{m27}$	2.31274(9)	6(1)	5.3	...
$f_{m28}$	2.2569(1)	6(1)	5.3	...
$f_{m29}$	2.30169(9)	6(1)	5.1	...

show the same time-delay signal with a period of more than 1400 days, as shown in Figure 3. The result suggests that KIC 3440495 is a pulsator in a binary system with an orbital period longer than the time span of the KLC data. The asymmetric time-delay curve implies that the orbit of the binary system has high eccentricity (Murphy & Shibahashi 2015; Murphy et al. 2016).

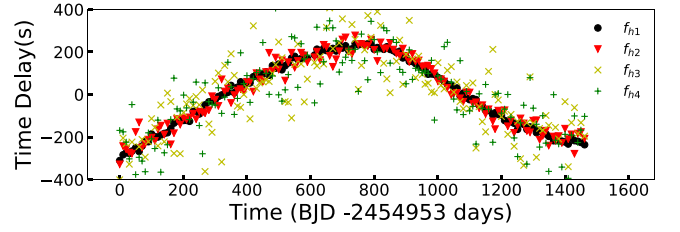


**Figure 3.** The time-delay measurements of the four high frequencies, using 10 day light-curve segments.

KIC 3440495 was observed by both the Kepler and TESS missions. There are expected to be phase shifts of the pulsations between the Kepler and TESS data due to the different passbands of the observations used by the two missions. Even in the absence of binarity, the pulsation phases in the Kepler and TESS data would not be identical. It is therefore non-trivial to combine the two data sets for a phase modulation analysis, and we do not attempt that here. We tried to determine the possible orbital parameters of the binary system based on these segments of the KLC data by using a Markov Chain Monte Carlo (MCMC) software program (Murphy et al. 2016; Hey et al. 2020). However, because the orbital period is longer than the time span of the data set, this fit is poorly constrained and there are many degenerate solutions for the orbital parameters (especially the orbital period and projected semimajor axis of  $a_1 \sin i/c$ ) (Murphy et al. 2016; Hey et al. 2020). Good solutions can still be obtained, but they are not the only solutions. Figure 4 displays the time-delay measurements of the dominant high frequencies  $f_{h1}$  by using multiple 10 day light-curve segments, and one of the best-fitting models for the time delay. One example solution acquired by the MCMC program gives an orbital period of  $2414^{+100}_{-110}$  days, a projected semimajor axis of  $a_1 \sin i/c = 339^{+14}_{-12}$  s, eccentricity of  $e = 0.35^{+0.03}_{-0.025}$ , and a mass function of  $f(m_1, m_2, \sin i) = \frac{(m_2 \sin i)^3}{(m_1 + m_2)^2} = 0.0067^{+0.0007}_{-0.0005} M_\odot$  (Murphy et al. 2016; Hey et al. 2020, 2022).

#### 4.2. A Rapidly Rotating Pulsator with Starspots

In Section 3.1, we attributed the frequency  $f_{m2}$  to rotational modulation. Here we analyse the consequences of this identification. It is reported that KIC 3440495 has a projected rotation velocity  $v \sin i$  of  $239(27)$  km s<sup>-1</sup> and an estimated radius of  $2.4(7) R_\odot$  based on the LAMOST spectrum with a high S/N in Section 1. The rotation period obtained from the KLC data by reciprocating the rotation frequency is  $P_{rot} = 0.430495(1)$  days ( $f_{rot} = 2.322909(2)$  day<sup>-1</sup>). Using the radius of  $2.4(7) R_\odot$ , the equatorial rotation velocity corresponding to this rotation period is  $280(80)$  km s<sup>-1</sup>. This velocity is consistent with the measured projected rotation velocity. The star is therefore oblate with such rapid rotation (Royer et al. 2007). The tidal effect from the binary companion is negligible due to the very long orbital period. Despite the oblateness, the star should remain axisymmetric, which should not give rise to any modulation by rotation. So there should be other reasons for the rotation modulation.

In the frequency analysis of the Kepler and TESS data, the star shows rotation modulation for a long time. The brightness variations of the star should be further analysed after excluding the disturbance of the pulsations. The KSC and KLC data will be used simultaneously to explore causes of the rotation

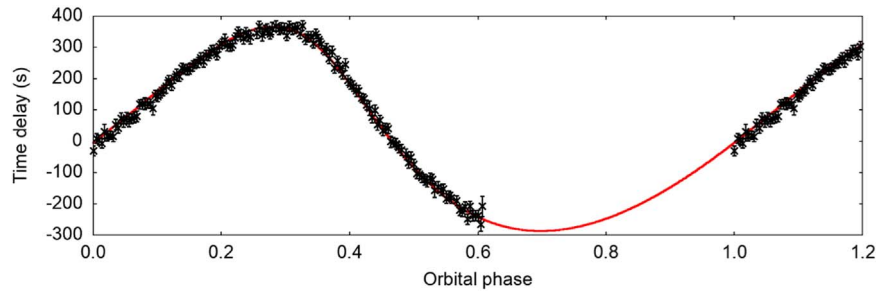


**Figure 4.** The time-delay measurements of the dominant high frequencies  $f_{h1}$  by using multiple 10 day light-curve segments, and one of the best-fitting models for the time delay.

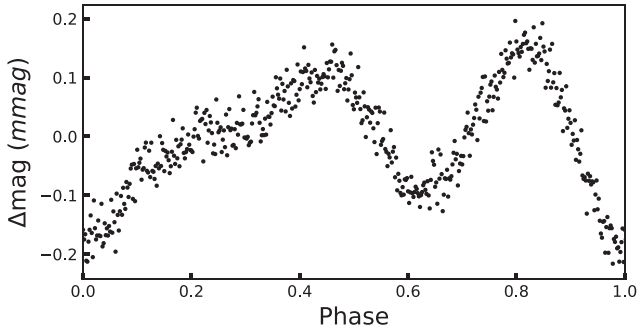


**Figure 5.** The phase folded light curve of KIC 3440495 with a period of 0.430495(1) days in the KSC data. The phase is binned every 0.002 phase.

modulation. First, we filter out all the pulsation frequencies independent of rotation with a S/N higher than 5 from the light curve of the KSC data, and fold the residuals of the light curve with the rotation frequency  $f_{\text{rot}} = 2.322909(2) \text{ day}^{-1}$ . The folded phase light curve is binned every 0.002 phase, and showed in Figure 5. It can be seen that the brightness of the star shows irregular variations during one rotation period. The feature of the brightness variations is usually seen in stars with starspots on the surface (Davenport et al. 2015).

To observe the brightness variations caused by possible starspots, we filter out all the pulsating frequencies independent of rotation with a S/N higher than 5 in the KLC data, and use the residuals to analyse the rotation modulation. The amplitude spectrum of the residuals is shown in Figure 6. We divide the residuals of the KLC data (1470.5 days) into five segments based on a time span of 300 days, and reextract the frequencies associated with the rotation. There are some gaps without data at the beginning and end of the segments, and the actual time span of each segment is 300 days, 299 days, 285 days, 300 days, and 271 days, in chronological order. The rotation frequency and its harmonics in each segment are listed in Table 4. It can be found that the amplitudes, phases, and S/R of the frequencies detected from each segment are different. The exact measurement of the rotation frequency,  $f_{\text{rot}} = 2.322909(2) \text{ day}^{-1}$ , is used to fold the light curve of each segment. The phased light curve and the amplitude spectra in each segment are displayed in Figure 7. Based on the phased light curve of each segment, it is inferred that there are several spots on the star’s surface, and these spots evolve over time. The harmonics of the rotation frequency are explained by the non-sinusoidal components of the phased light curve.

To get more information about these significant starspots, the rotation frequency  $f_{\text{rot}} = 2.322909(2) \text{ day}^{-1}$  is used to fold the whole light curve of the residuals, and a continuous phase

evolution diagram over a time span of about four years is shown in Figure 8. The data are folded twice in phase for visual clarity. In Figure 8, each row of pixels spans 0.05 in phase, and each column contains data spanning 10 days in time. The shading corresponds to the median value for the flux within each (time, phase) pixel. The pixel shades, from dark to light, indicates the median flux from low to high. We can see that the brightness on the star’s surface is uneven over one phase range from this diagram. The dark regions in the diagram may represent prominent starspots. These prominent spots evolve gradually in time from left to right according to Figure 8.

Rotational modulation at different time intervals is possibly due to different starspots, which may result in slight variations in the measurements of the rotational frequency and its harmonics including their phases. In addition, it can be found that these prominent starspots have a lifetime of a few hundred days and cover large regions on the surface of the star. Such large and long-lasting starspots are usually found only in stars with lower temperatures such as M/G/K-type stars (Giles et al. 2017), but large-scale bright spots have also been proposed for A-type stars (Braithwaite & Cantiello 2013). However, each prominent “star spot” in Figure 8 might be a cluster of many small starspots on the stellar surface. New starspots might appear while some starspots disappear in the clusters. Therefore, viewed as a whole, these clusters are relatively stable over a long time span.

Recent studies have shown that many A-type stars observed by Kepler and TESS have noteworthy rotational modulations similar to the surface features of stellar spots (Balona 2018, 2019, 2021). In fact, some A-type stars have been detected to have weak magnetic fields, such as Vega and Sirius (Petit et al. 2010; Blazère et al. 2016), and the presence of starspots has been confirmed on the surface of a few A-stars (Böhm et al. 2015; Savanov 2019). KIC 3440495 is not an isolated case. Maeder & Meynet (2004) considered that differential rotation may produce a dynamo in radiative layers that generate a magnetic field. Many A/F stars are moderate-to-fast rotators (Royer et al. 2007; Zorec & Royer 2012), and this mechanism may be responsible for the magnetic field of these stars. Other studies have suggested that magnetic fields in A-type stars may be failed fossil fields which are evolving dynamically toward a “fossil” equilibrium but have not yet arrived there (Braithwaite & Cantiello 2013), or dynamo-generated magnetic fields which originate in the subsurface convective layer driven by second helium ionization (Cantiello & Braithwaite 2019). According to Braithwaite & Cantiello (2013) and Cantiello & Braithwaite (2019), failed fossil fields should be relatively inactive with only larger scales, while dynamo-generated magnetic fields may have small scales and

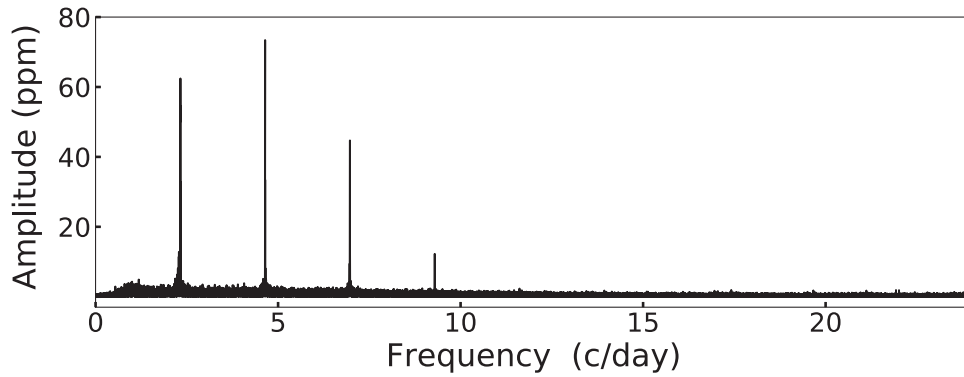


**Figure 6.** The amplitude spectrum of the residuals after filtering out all the significant pulsating frequencies ( $S/N \geq 5$ ) independent of rotation in the KLC data, but leaving the rotation frequency and its harmonics.

**Table 4**

Frequencies Extracted from Each Segment of the Residuals of the KLC Data

Segment	Number	Frequency (day <sup>-1</sup> )	Amplitude (ppm)	Phase	S/N
Segment 1	$f_{\text{rot}}$	2.32247(4)	73(2)	0.288(3)	23.7
	$2f_{\text{rot}}$	4.64443(9)	57(3)	0.85(3)	24.2
	$3f_{\text{rot}}$	6.96807(4)	79(2)	0.195(3)	40.8
	$4f_{\text{rot}}$	9.291(9)	10(3)	0.6(1)	6.3
Segment 2	$f_{\text{rot}}$	2.32455(4)	64(1)	0.619(3)	23.6
	$2f_{\text{rot}}$	4.64665(2)	110(1)	0.034(2)	47.7
	$3f_{\text{rot}}$	6.96893(6)	48(1)	0.816(5)	25.4
	$4f_{\text{rot}}$	9.2919(7)	22(3)	0.29(6)	14.9
Segment 3	$f_{\text{rot}}$	2.32245(3)	102(1)	0.064(2)	34.9
	$2f_{\text{rot}}$	4.64534(3)	101(1)	0.906(2)	44.5
	$3f_{\text{rot}}$	6.9698(2)	18(1)	0.57(1)	9.2
	$4f_{\text{rot}}$	9.2920(2)	18(1)	0.30(1)	11.8
Segment 4	$f_{\text{rot}}$	2.32378(3)	100(2)	0.45(2)	33.4
	$2f_{\text{rot}}$	4.64589(4)	75(2)	0.3(2)	31.7
	$3f_{\text{rot}}$	6.96912(7)	44(1)	0.10(7)	22.6
	$4f_{\text{rot}}$	9.2923(2)	14(2)	0.93(2)	9.0
Segment 5	$f_{\text{rot}}$	2.3239(2)	124(2)	0.37(1)	41.3
	$2f_{\text{rot}}$	4.65(2)	79(3)	0.4(1)	32.3
	$3f_{\text{rot}}$	6.97(5)	69(3)	0.8(2)	32.8
	$4f_{\text{rot}}$	9.29(5)	7(2)	0.10(4)	4.7

rapidly evolving features that are constantly regenerated. The long-term existence of large clusters of starspots suggests that KIC 3440495 may have a relatively active magnetic field. So the large clusters of starspots may be the result of a dynamo-generated magnetic field. Although these above views seem to provide a plausible explanation for the presence of starspots on A-type stars, there are still many doubts that need to be further verified. It is believed that these insights will contribute to our understanding of the envelopes of high-temperature stars.

#### 4.3. Studying the Large Separation

Although  $\delta$  Sct stars do not pulsate in the asymptotic regime, there exists several works related to the search for large separations in their pulsation spectra since the end of the twentieth century (Handler & Breger 1997; Breger et al. 1999; García Hernández et al. 2009, 2013; Paparó et al. 2016; Bedding et al. 2020). The revolution came with the establishment of a relation between this large separation in the low-order regime and the stellar mean density, from modeling

(Reese et al. 2008; Suárez et al. 2014; Ouazzani et al. 2015) and, specially, from observations (García Hernández et al. 2015, 2017; Bedding et al. 2020; Hasanzadeh et al. 2021). It was demonstrated that this relation is invariant to rotation (Reese et al. 2008; García Hernández et al. 2015), although the value of  $\Delta\nu$  itself does change from a nonrotating to a rotating star of the same mass. This result allows to obtain reliable mean densities of fast rotating  $\delta$  Sct stars, such as KIC 3440495.

To find  $\Delta\nu$  in fast rotating stars it is unsuitable to use échelle diagrams alone because the usual distribution of frequencies changes compared to the nonrotating case (Lignières et al. 2006; Reese et al. 2006), suggesting new classes of pulsating modes (Lignières & Georgot 2008, 2009). A better approach is thus to use statistical methods. We follow the methodology of García Hernández et al. (2009, 2013) and Ramón-Ballesta et al. (2021), using a FT, the autocorrelation function (AC), and a histogram of frequency differences (HFD) to find a pattern in the frequency set of KIC 3440495. To compute these transformations, all the amplitudes have been normalized to one.

In Figure 9, we plot the FT, AC, and HFD in one single plot. The star is a  $\delta$  Sct- $\gamma$  Dor hybrid pulsator, whose amplitude spectrum shows significant peaks in the range 0.5–24.3 day<sup>-1</sup>. The large separation is expected to be found in p modes, and the p modes in  $\delta$  Sct stars are usually above 5 day<sup>-1</sup> (Grigahcène et al. 2010). Therefore, we selected frequencies higher than 5 day<sup>-1</sup> to include possible p modes and removed the rotational harmonics in that range from the full list of frequencies. All the transforms show a prominent peak at around 2.33 day<sup>-1</sup> (27  $\mu$ Hz), which is exactly the rotation, marked with a red line. Other peaks at larger values do not coincide in the three methods. The AC and the HFD, which in general follow the same distribution, have a maximum value around 6.74 day<sup>-1</sup> (78  $\mu$ Hz) that is 3 times the rotation frequency. All this points to the possible case in which the rotation frequency is half the large separation value. In fact, this is something expected from theory (Reese et al. 2017a) and has also been found in observations, in the case of Rasalhague (Ramón-Ballesta et al. 2021), for stars rotating around  $0.7\Omega_K$ , where  $\Omega_K$  is the rotation frequency at which the centrifugal force exactly compensates for equatorial gravity.<sup>9</sup> In fact, this might be the case of KIC 3440495 since it

<sup>9</sup> We must differentiate between the critical rotation rate and the Keplerian rotation rate, the latter of which is the one used here. The former is the rotation at breakup, i. e., when the star has a shape due to centrifugal deformation in which it starts to lose mass. The latter is the rotation that equals the gravity force and the centrifugal force at the equator for a given star, so this case do not suppose any additional deformation. Usually, the critical rotation rate is smaller than the Keplerian rotation rate.



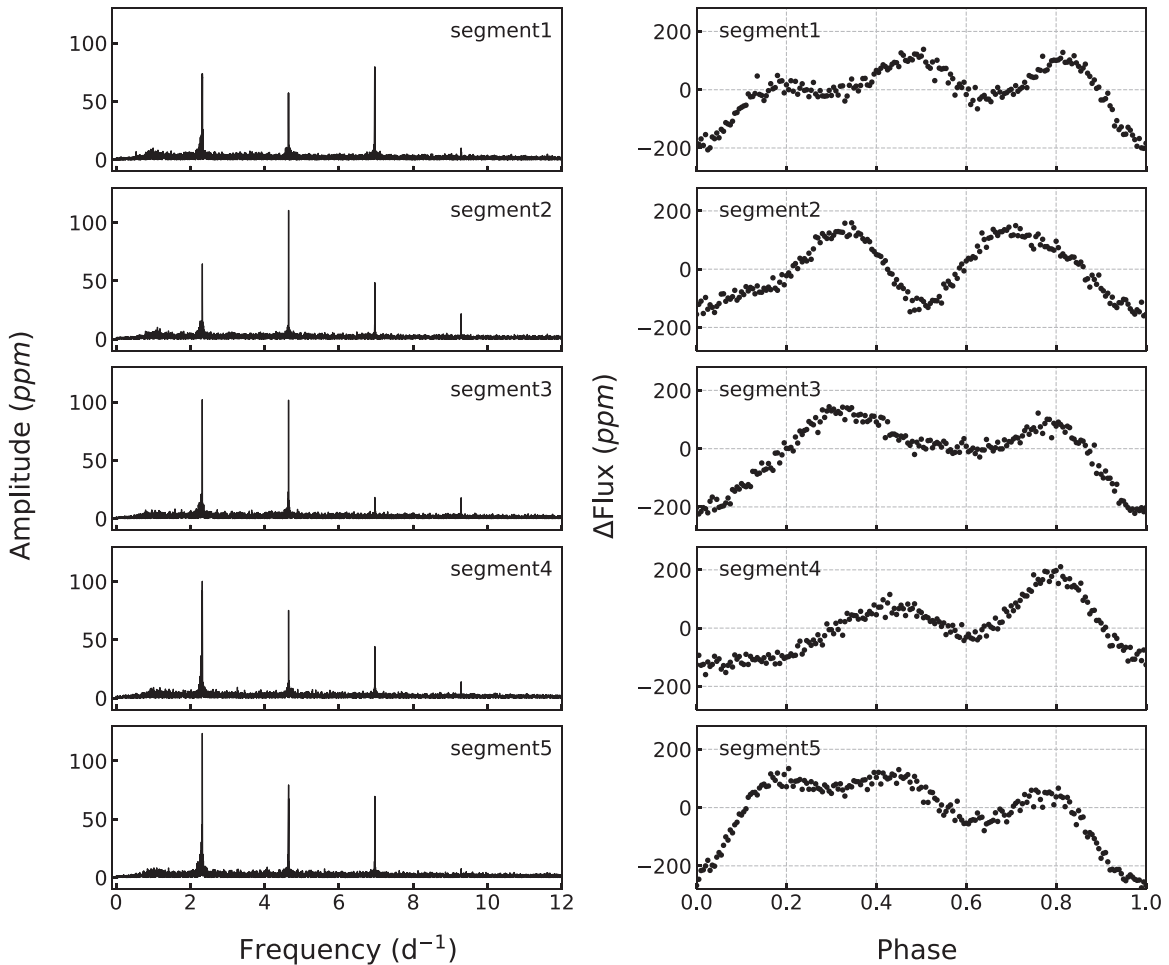


**Figure 7.** The amplitude spectra and phase folded light curves of each segment. The phases are binned every 0.002 phase.

is the case of Altair ( $0.75 \Omega_K$ ). It should be noted that, according to Reese et al. (2017a), the coincidence of a semi-large separation and rotational rate only occurs when the star rotates at about  $0.3 \Omega_K$  or  $0.7 \Omega_K$ . If a star rotates at other rates, such a coincidence does not occur. Therefore, such a coincidence is reached only by chance.

Using  $\Delta\nu = 54.5 \mu\text{Hz}$ , we can see a clear ridge in the échelle diagram in Figure 10 (Bedding et al. 2020; Hasanzadeh et al. 2021). We can check the validity of this large separation and obtain more information about KIC 3440495 with some simple calculations. From now on, we must think of it as an oblate star, and distinguish between the polar and equatorial radius. Additionally, the shape of the star is assumed to follow a Roche model (Maeder 2009). First, the mean density corresponding to this large separation can be obtained with the formula of García Hernández et al. (2017) and thus  $\rho = 0.33(3) \text{ g cm}^{-3}$ . Second, we can obtain a minimum value of the equatorial radius just from the projected rotational velocity if this was the true rotational velocity and the rotational frequency. This gives an equatorial radius of  $R_{\text{equator}} = 2.03 R_{\odot}$ . With the equatorial radius and the Roche model, we can calculate the stellar volume but we need first an estimation of  $\omega = \Omega/\Omega_K$  with  $\Omega_K = (GM/R_{\text{equator}}^3)^{1/2}$  (Maeder 2009). This  $\omega$  is a measure of the stellar deformation. To compute this quantity we need the mass. As a first guess we can take the maximum of the measured values plus the uncertainties (the maximum is needed to get the minimum radius), that is  $M = 2.1 M_{\odot}$  (Table 1).

Using the mean density, we can calculate a new value of the mass and go again, in an iterative process, to refine  $\Omega_K$  and the mass. These are the final values we find:  $M = 1.65 M_{\odot}$  and  $\omega = 0.61$ . Third, in the similar way but using the lowest measured stellar mass (Table 1), we can limit the upper value of the radius and  $\Omega_K$ . Thus, if  $M = 1.5 M_{\odot}$ , we can compute the stellar volume with the mean density and a mean radius, use it to compute a first guess of  $\Omega_K$  and the Roche model then to compute the equatorial radius. With an iterative process again, we can use this new equatorial radius to refine  $\Omega_K$  and go again for the Roche model. In that way, we obtain upper values of  $R = 2.30 R_{\odot}$  and  $\omega = 0.77$ . With these values and the rotation frequency, it is also possible to determine the unprojected rotational velocity as  $v = 279 \text{ km s}^{-1}$ . Moreover, once  $R_{\text{equator}}$  and  $\omega$  are determined, the polar radius,  $R_{\text{polar}}$  can also be calculated using Equation (38) from Paxton et al. (2019), so the stellar shape is characterized. So the refined stellar parameters according to these calculations are  $v = [239, 279] \text{ km s}^{-1}$ ,  $M = [1.5, 1.65] M_{\odot}$ ,  $R_{\text{equator}} = [2.03, 2.30] R_{\odot}$ ,  $R_{\text{polar}} = [1.72, 1.78] R_{\odot}$ , and  $\omega = [0.61, 0.77]$ .

All the quantities previously calculated are compatible with the values obtained from other methodologies. That is not the case if we use other possible values of the large separation, such as  $80 \mu\text{Hz}$ . We tested this case and also the  $62 \mu\text{Hz}$  value (as a prominent peak also in the AC function) to check their compatibility with the observations. With these values, we ended with unprojected rotational velocities that are under the measured

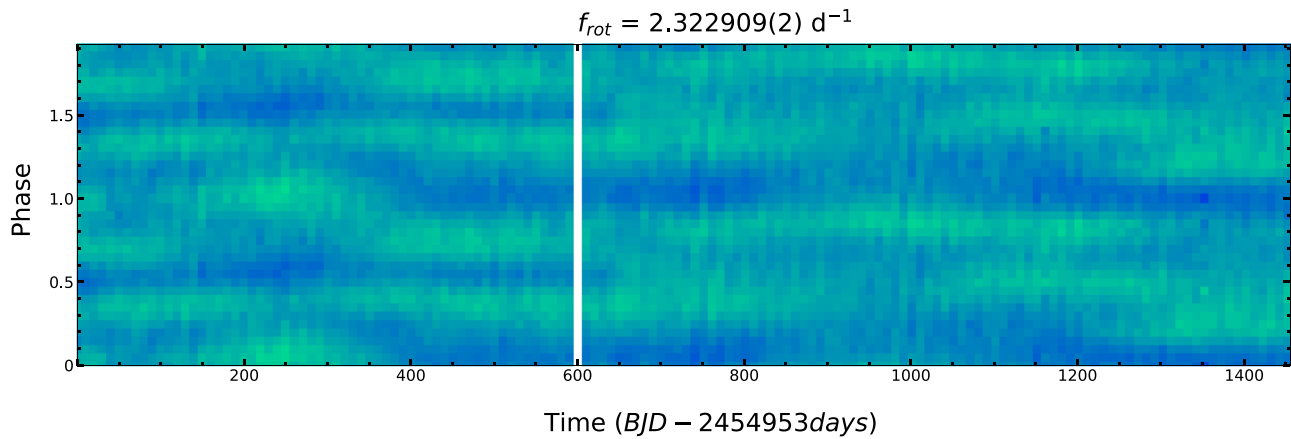


**Figure 8.** The phase evolution diagram over a time span of about four years for the residuals of the KLC data. Pixel shades, from dark to light, indicate the median flux in each (time, phase) bin from low to high. The pixels span 10 days in time and 0.05 in phase. The vertical white gap corresponds to a time span without Kepler data. The brightness can be seen to be uneven in one phase range from this diagram and to evolve gradually in time from left to right. The dark regions in the diagram can be seen as starspots on the surface of the star.

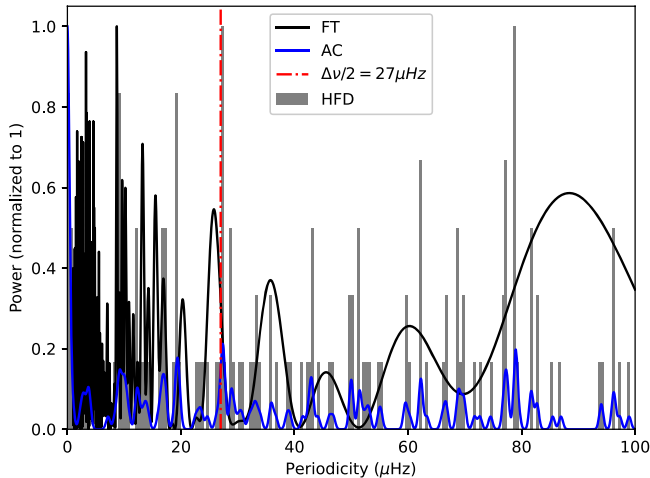


**Figure 9.** A prominent peak marked with a red line is displayed in the FT, AC, and HFD. The peak is around  $2.33 \text{ day}^{-1}$  ( $27 \mu\text{Hz}$ ) corresponding to the rotation. The other peaks at larger values do not coincide in the three methods. But there is a maximum value around  $6.74 \text{ day}^{-1}$  ( $78 \mu\text{Hz}$ ), which is 3 times the rotation frequency in the AC and HFD.

value. So we can discard them as plausible values of  $\Delta\nu$ . We cannot go further in the analysis, such as doing mode identification, for example, because we would need 2D models to account for such stellar deformation.

#### 4.4. A Potential Sister of Altair

In the literature, it is found that KIC 3440495 is very similar to the widely studied star Altair (Suárez et al. 2005; Bouchaud et al. 2020; Le Dizès et al. 2021). Interestingly, the oscillation spectrum of KIC 3440495 shows many similarities with that of Altair. The amplitude spectra of KIC 3440495 and Altair are presented as a comparison in Figure 11. The data of Altair’s spectrum are from the Microvariability and Oscillations of STars (MOST) satellite from 2012 (see Le Dizès et al. 2021). The two stars coincidentally exhibit very close excited modes at low and high frequencies. The three frequencies with the highest amplitude are  $15.9733 \text{ day}^{-1}$ ,  $0.6364 \text{ day}^{-1}$ , and  $20.29943322 \text{ day}^{-1}$  in the KIC 3440495 spectrum, and  $15.7679 \text{ day}^{-1}$ ,  $0.57 \text{ day}^{-1}$ , and  $20.7865 \text{ day}^{-1}$  in the Altair spectrum.

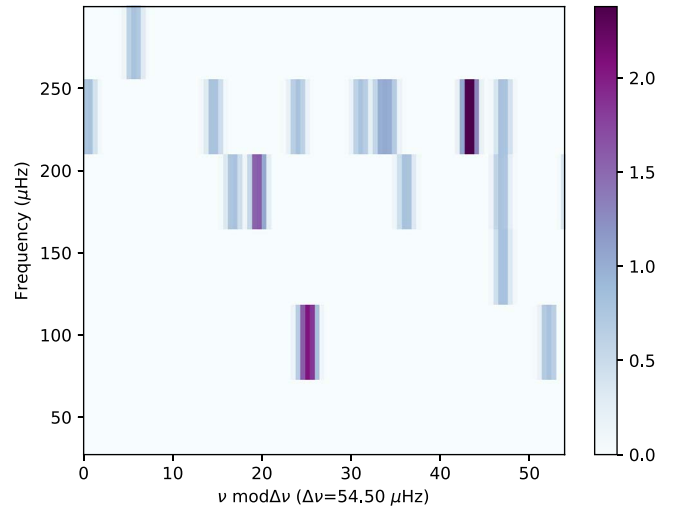


**Figure 10.** The échelle diagram with a frequency spacing of  $\Delta\nu = 54.5 \mu\text{Hz}$  shows a clear ridge, which infers  $\Delta\nu$  is the possible large separation.

There are four frequencies larger than  $25 \text{ day}^{-1}$  detected in the Altair spectrum, but no frequency in the range  $25\text{--}80 \text{ day}^{-1}$  has been found in our work on KIC 3440495. All the frequencies detected from the Altair spectrum are listed in Table 5 and compared with the close frequencies detected from the spectrum of KIC 3440495.

In addition, these two stars have many similarities in other aspects. The effective temperature of KIC 3440495 in TIC is 7596 (140) K derived from photometric measurements, which is very close to the average effective temperature of 7550 K for Altair derived in the same way (Erspamer & North 2003). Altair is also a rapidly rotating  $\delta$  Sct at a distance of 5.13(2) pc (van Leeuwen 2007), and is identified as an oblate star by using near-infrared interferometric observations (van Belle et al. 2001; Domiciano de Souza et al. 2005; Monnier et al. 2007). Reiners & Royer (2004) derived a  $v \sin i$  of  $227(11) \text{ km s}^{-1}$  from spectroscopic studies, which is close to that of KIC 3440495. Other measurements of  $v \sin i$  of Altair are also reported in the range  $190\text{--}250 \text{ km s}^{-1}$  (Royer et al. 2002; Bouchaud et al. 2020).

Different stellar models have been developed for studying the structure and evolution of Altair (Domiciano de Souza et al.

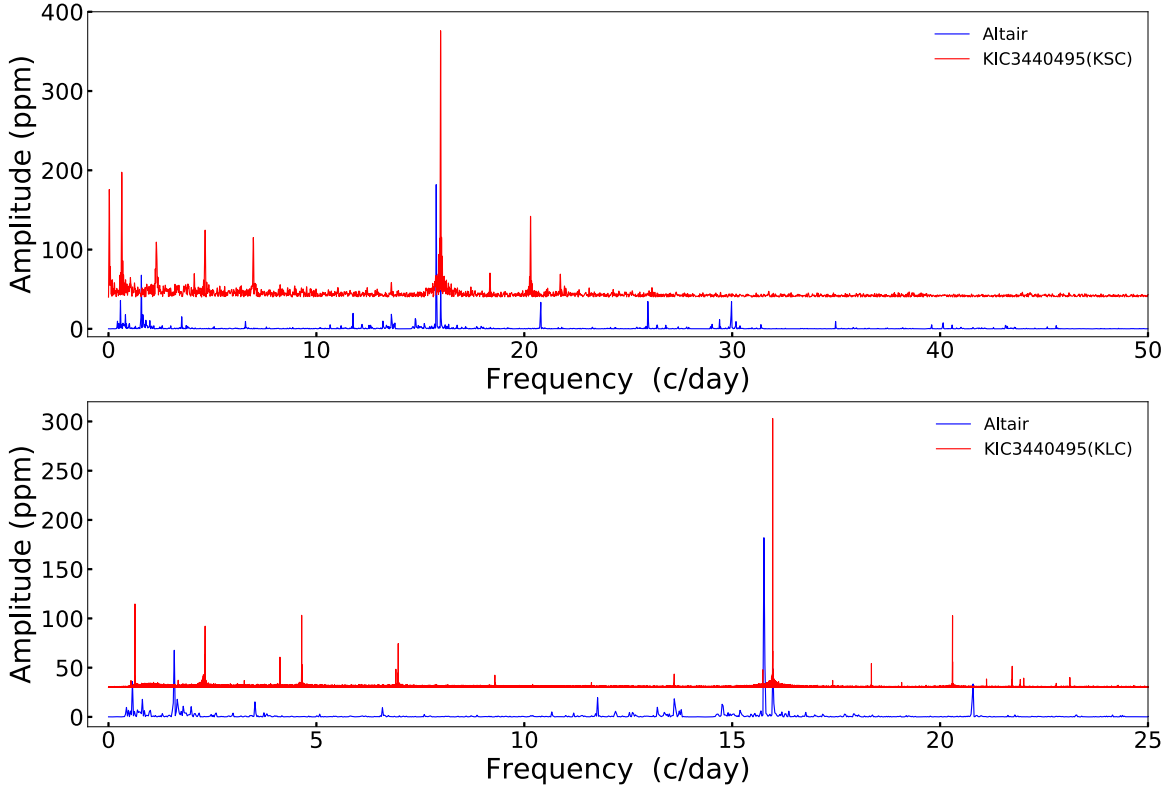


**Figure 11.** The amplitude spectra of KIC 3440495 from Kepler data and Altair from MOST data from 2012. KSC and KLC are the abbreviations for Kepler short and long cadence, respectively.

**Table 5**

The Contrast of Pulsation Frequencies of Altair and KIC 3440495

Altair (Le Dizès et al. 2021)		KIC 3440495	
Frequency (day <sup>-1</sup> )	Amplitude (ppm)	Frequency (day <sup>-1</sup> )	Amplitude (ppm)
0.57	270	0.54088(7)/ 0.636467(6)	8(1)/85(2)
0.81	160	1.0819(1)	6(2)
1.66	200	1.67624(7)	7(1)
2.58	100	2.323181(8)	68(1)
3.527	150	3.26635(9)	6(1)
15.7679	520	15.73522(3)	16(1)
15.983	260	15.973311(7)	272(1)
16.180	140	15.9752(1)	2(2)
17.93	80	17.41632(8)	7(1)
20.7865	330	20.299433(7)	73(1)
23.28	110	23.12028(5)	10(1)
25.952	220	...	...
28.408	120	...	...
29.04	100	...	...
35.82	80	...	...

**Note.** The frequencies of Altair are from Le Dizès et al. (2021). Based on the literature, the uncertainties on these frequencies are typically 0.02 day<sup>-1</sup> or better. The amplitudes are average values since they vary in time (Le Dizès et al. 2021).

2005; Bouchaud et al. 2020). Considering gravity darkening caused by fast rotation, the oblateness induces a difference in the effective temperature between the equator and the poles. The recent 2D model of Bouchaud et al. (2020) shows the different temperatures and radii of the equator ( $R_{\text{equator}}$ ) and

**Table 6**

Parameters of Altair

Parameters	Value in TIC	References
R.A.	+19 <sup>h</sup> :50 <sup>m</sup> :47 <sup>s</sup> .00	
Decl.	+08 <sup>o</sup> :52′:05″.96	
log $g$	4.1(3) dex	(a)
$T_{\text{eff}}$	7550(200) K	(a)
$T_{\text{polar}}$	8621(55) K	(b)
$T_{\text{equator}}$	6780(40) K	(b)
$M$	1.86(3) $M_{\odot}$	(b)
$R_{\text{polar}}$	1.57(1) $R_{\odot}$	(b)
$R_{\text{equator}}$	2.008(6) $R_{\odot}$	(b)
$v_{\text{equator}}$	313 km s <sup>-1</sup>	(b)
$v \sin i$	242 km s <sup>-1</sup>	(b)
$Z$	0.019	(b)
$[M/H]$	0.19	(b)
$X_c$	0.71	(b)
$L$	10.2(1) $L_{\odot}$	(b)
Distance	5.13(2) pc	(c)

**Note.** (a) Erspamer & North (2003). (b) Bouchaud et al. (2020). (c) van Leeuwen (2007).

pole ( $R_{\text{polar}}$ ) for Altair, who deduce an equatorial velocity of about 313 km s<sup>-1</sup>. The  $R_{\text{equator}}$  of Altair is within the estimated range of  $R_{\text{equator}}$  for KIC 3440495, and the  $R_{\text{polar}}$  of Altair is below the estimated range of  $R_{\text{polar}}$  for KIC 3440495 in Section 4.3. This implies that KIC 3440495 may not be as oblate as Altair. The true luminosity of Altair could be 10.2(1)  $L_{\odot}$  according to the concordance model of Bouchaud et al. (2020), which is equal to that of KIC 3440495 in TIC, 10.2(5)  $L_{\odot}$ . Using stellar interior and atmosphere models constrained

by observations of interferometry, spectroscopy, and photometry, the mass of Altair ( $M_{\text{Altair}}$ ) is determined to  $1.86(3) M_{\odot}$ , and its metallicity and the mass fraction of its core hydrogen are deduced to be  $Z=0.019$  and  $X_c=0.71$ , respectively (Bouchaud et al. 2020).  $M_{\text{Altair}}$  is bigger than the maximum value of the mass of KIC 3440495 obtained by using the large separation in Section 4.3. Based on the results of the models, Altair is proposed to be a young star with an age about 100 Myr (Bouchaud et al. 2020). The results of the 2D model are listed in Table 6, including some other parameters from the literature.

KIC 3440495 is a potential sister of Altair, and probably is at a similar stage of evolution and approximate fundamental parameters. Pulsators with very similar oscillation spectra like those of KIC 3440495 and Altair are very rare and interesting. In addition, there are many other similar properties and some differences between the two stars. It is essential to model this star using the same (or similar) 2D model as Altair in order to explore intrinsically the differences between the two stars.

## 5. Summary

We analysed the Kepler and TESS data of KIC 3440495, and confirmed that the star is a  $\delta$  Sct- $\gamma$  Dor hybrid pulsator. It is inferred that the star is in a binary system with a period longer than the time span of the KLC data, according to the pulsational phase modulations. A set of possible parameters for the binary star system were estimated by fitting the time-delay measurements of the dominant high frequency  $f_{h1}$ . KIC 3440495 shows low and high pulsating frequencies along with one rotation frequency and four harmonics in the KLC data. The rotation frequency is derived to be  $f_{\text{rot}}=2.322909(2) \text{ day}^{-1}$  ( $P_{\text{rot}}=0.430495(1) \text{ days}$ ), and the rotational modulation is determined to be caused by starspots. In support of this hypothesis, we have presented evidence of brightness variations at a fixed rotational frequency with apparent lifetimes of a few hundred days. In addition, we found a frequency separation of  $\Delta\nu=54.5 \mu\text{Hz}$  that is about twice the rotation frequency, by using FT, AC, HFD, and an échelle diagram. The stellar parameters of the star were estimated from its large separation.

According to the similarities in the amplitude spectrum and in its physical parameters (luminosity, effective temperature, and rotational velocity), KIC 3440495 is a potential sister of Altair. The two stars are probably at the same stage of evolution. Altair is an extensively studied  $\delta$  Sct star, and its evolutionary stage and fundamental parameters have been well determined using interferometry. Based on the studies of Altair, KIC 3440495 is inferred to be a young star.

Fast rotation can distort the stellar surface and disarrange the oscillation spectrum of a pulsator among the intermediate-mass MS stars (Deheuvels et al. 2015; Reese et al. 2017b; Mirouh et al. 2021). This effect skews the observed parameters, which increases the difficulty of understanding these stars. As a fast rotating  $\delta$  Sct, KIC 3440495 is an interesting target as it displays a rich oscillation spectrum that will help us constrain its fundamental parameters. Further studies on KIC 3440495 are necessary in order to understand better the effect of rotation on stellar evolution. 2D models like ESTER (Espinosa Lara & Rieutord 2013; Rieutord et al. 2016) should be used for modeling it, as well as for the computation of its amplitude spectrum (Reese et al. 2021). We aim to construct these models in future work.

We thank the anonymous referee for the helpful comments, which improved the manuscript. We also thank Paparo Margit and Daniel Reese for advice on some issues. This research is supported by the National Natural Science Foundation of China (grant Nos. 12003060 and U2031209), the Natural Science Foundation of Xinjiang Uygur Autonomous Region (grant No. 2020D01B59), and the Chinese Academy of Sciences (CAS) ‘‘Light of West China’’ Program (grant No.2021-XBQNXX-029). A.G.H. acknowledges support from ‘‘FEDER/Junta de Andalucía-Consejería de Economía y Conocimiento’’ under project E-FQM-041-UGR18 by Universidad de Granada. J.P.G. acknowledges funding support from Spanish public funds for research from project PID2019-107061GB-C63 from the ‘‘Programas Estatales de Generación de Conocimiento y Fortalecimiento Científico y Tecnológico del Sistema de I+D+i y de I+D+i Orientada a los Retos de la Sociedad’’, and from the State Agency for Research through the ‘‘Center of Excellence Severo Ochoa’’ award to the Instituto de Astrofísica de Andalucía (SEV-2017-0709), all from the Spanish Ministry of Science, Innovation and Universities (MCIU). We would like to thank the Kepler science team and the TESS mission for providing such excellent data. This work has made use of data products from the Guoshoujing Telescope (the Large Sky Area Multi-Object Fiber Spectroscopic Telescope, LAMOST). This research made use of *Lightkurve*, a Python package for Kepler and TESS data analysis.

## Appendix A

### The Simple Aperture Photometry of TPFs

In TESS mission, the TPFs are the rawest form of target-specific data that are available at MAST. We use *Lightkurve* to access the TPFs of Sectors 40 and 41 for KIC 3440395 from MAST, respectively (Brasseur et al. 2019). The TPFs are  $20 \times 20$  pixel squares centered at KIC 3440395, and contain a stack of images for each observation cycle. By combining the fluxes in the pixels where KIC 3440395 appears, we can make a measurement of the amount of light from the star in that observation. The pixels chosen in this measurement are referred to as an aperture. Therefore, we first make an aperture mask and a background mask for the aperture photometry. The aperture mask is created using the thresholding method. This method will identify the pixels in TPFs which show a median flux that is brighter than the threshold times the standard deviation above the overall median. The standard deviation is estimated in a robust way by multiplying the median absolute deviation (MAD) by 1.4826. Figure 12 shows the target, aperture mask, and background mask used for the photometry in Sectors 40 and 41. In Figure 12, the color indicates the flux of each pixel in electrons per second. The y-axis shows the pixel rows, and the x-axis the pixel column. The title shows the serial number of the target and the observing cadence. Figure 13 shows the time-series flux variation of the target including background, only the background, and subtracting the background in each sector. The time-series flux variation of the target after subtraction of the background is the result of simple aperture photometry (SAP). The SAP fluxes contain some outliers and has no obvious trends. Hence, the SAP fluxes are used for the frequency analysis of KIC 3440495 without further correction after removing outliers. More details about the SAP can be seen in the tutorial of *Lightkurve*.

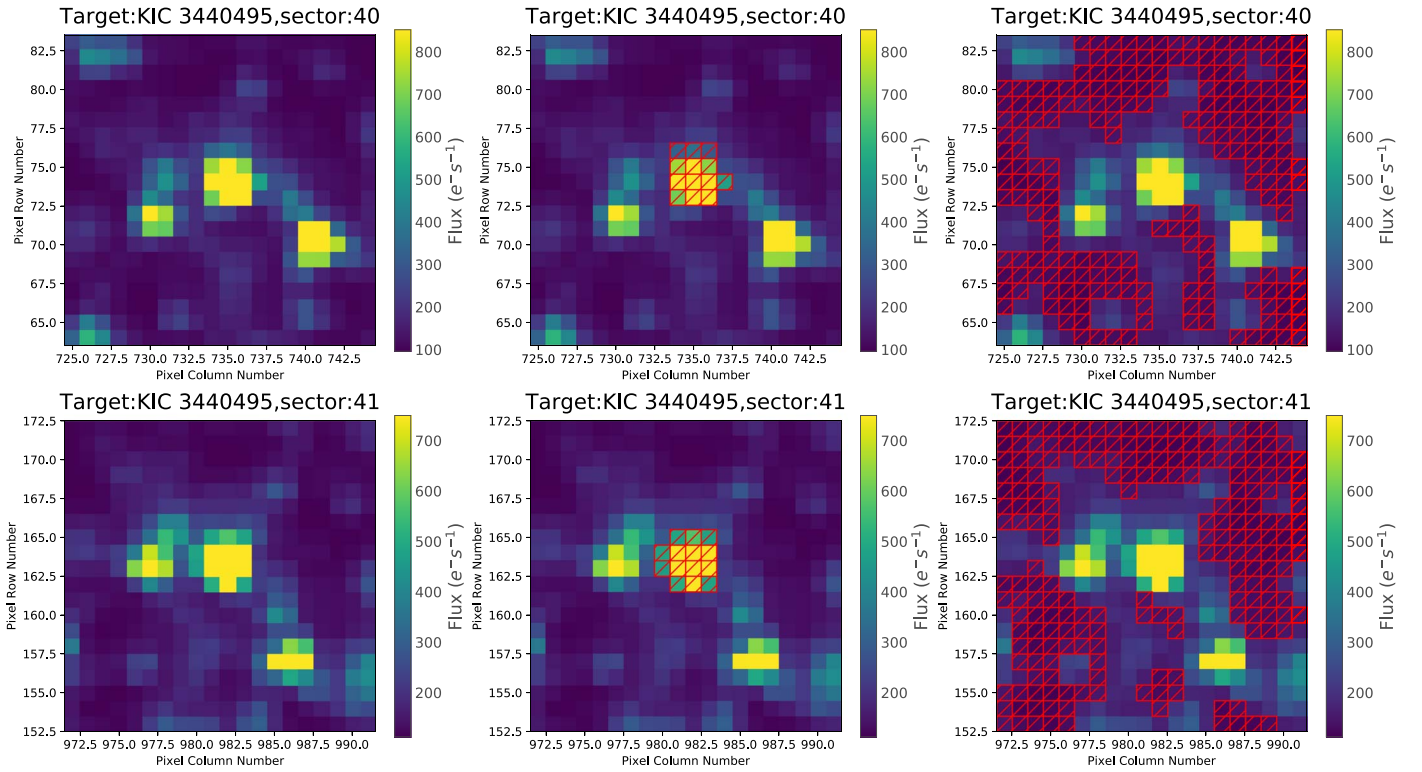


**Figure 12.** The TPFs of KIC 3440495 and the basic photometry mask. Top three panels: the target, the aperture mask, and background mask of S40 for the photometry from left to right. Bottom three panels: those of S41.

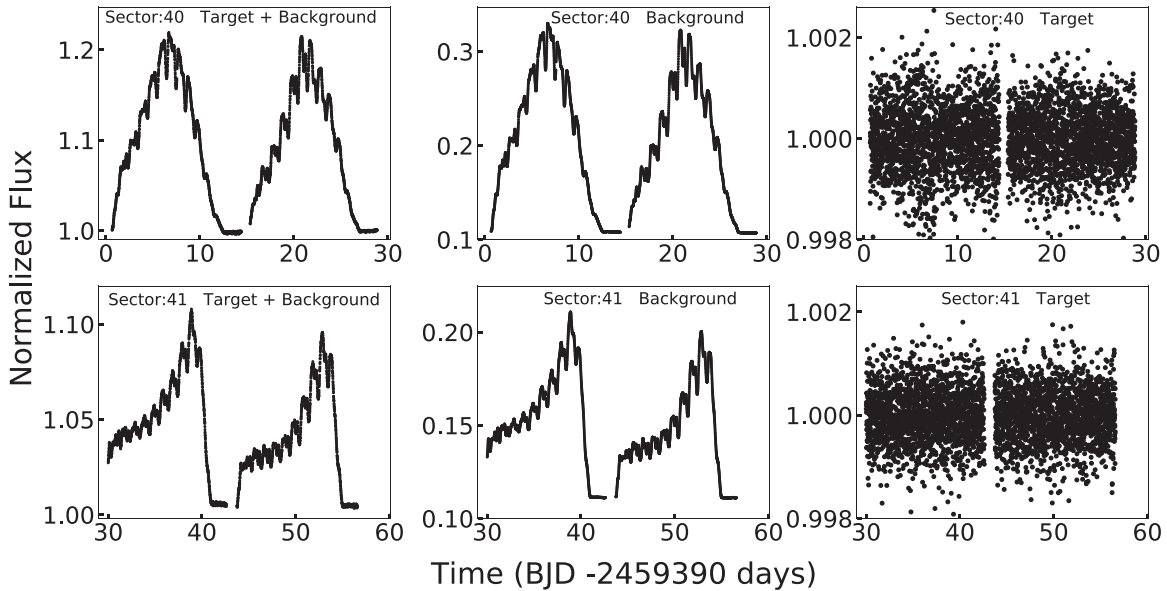


**Figure 13.** The light curves of KIC 3440495 in S40 and S41 obtained by using SAP. Top three panels: the time-series flux variation of the target with background, the time-series flux variation of the background, and the time-series flux variation after subtracting the background in S40 from left to right. Bottom three panels: the same for S41.

## Appendix B

### The Frequencies Extracted from Other Data Sets

In the paper, we use the Kepler and TESS datasets to analyze the characteristics of KIC 3440495. There are less significant frequencies in the datasets of KSC and TESS than those in the KLC data due to higher noises in these datasets than in the KLC data. These frequencies in these

datasets are in agreement with the frequencies in the KLC data within the allowed error range, and their sequence numbers are kept in line with those in the KLC data. The frequencies extracted from the KLC data are reported in Table 3, and the frequencies extracted from the datasets of KSC and TESS are listed in Tables 7, 8, and 9, respectively.

**Table 7**  
Frequencies Extracted from the KSC Spectrum

$f_i$	Frequency (day <sup>-1</sup> )	Amplitude (ppm)	S/N	Comment
$f_{h1}$	15.97314(7)	336(1)	133.9	$f_{p1}$
$f_{h2}$	20.2995(2)	101(1)	37.4	$f_{p2}$
$f_{h3}$	18.3484(8)	30(1)	11.1	...
$f_{h5}$	15.733(2)	19(1)	8.0	...
$f_{h4}$	21.731(2)	29(1)	7.6	...
$f_{h6}$	13.605(1)	19(1)	6.3	...
$f_{i1}$	0.6377(1)	158(1)	22.8	...
$f_i$	0.0379(2)	122(1)	17.9	...
$f_{i2}$	4.1261(9)	31(1)	5.3	...
$f_{m1}$	4.6467(7)	85(2)	15.4	$2f_{rot}$
$f_{m4}$	6.9674(3)	80(1)	15.1	$3f_{rot}$
$f_{m3}$	2.3005(5)	68(2)	10.1	$f_{rot}$


**Table 8**  
Frequencies Extracted from the TSC Spectrum

$f_i$	Frequency (day <sup>-1</sup> )	Amplitude (ppm)	S/N	Comment
$f_{h1}$	15.9732(4)	245(8)	23.7	$f_{p1}$
$f_{h2}$	20.2990(8)	105(10)	10.7	$f_{p2}$
$f_{h4}$	21.737(2)	43(10)	4.6	...
$f_{i7}$	3.265(2)	44(10)	3.5	...
$f_{m1}$	4.6443(8)	120(10)	12.0	$2f_{rot}$
$f_{m3}$	2.326(2)	46(8)	4.5	$f_{rot}$

**Table 9**  
Frequencies Extracted from the TLC Spectrum

$f_i$	Frequency (day <sup>-1</sup> )	Amplitude (ppm)	S/N	Comment
$f_{h1}$	15.973(1)	241(17)	11.7	...
$f_{h2}$	20.307(3)	101(15)	4.0	...
$f_{h11}$	17.703(5)	77(16)	4.3	...
$f_{m3}$	2.325(3)	130(17)	5.5	$f_{rot}$

## ORCID iDs

Shuguo Ma  <https://orcid.org/0000-0001-5066-5682>  
 Ali Esamdin  <https://orcid.org/0000-0003-1845-4900>  
 Simon J. Murphy  <https://orcid.org/0000-0002-5648-3107>  
 Chenglong Lv  <https://orcid.org/0000-0001-6354-1646>  
 Peng Wei  <https://orcid.org/0000-0002-5674-4223>  
 Michel Rieutord  <https://orcid.org/0000-0002-9395-6954>  
 Javier Pascual-Granado  <https://orcid.org/0000-0003-0139-6951>  
 TaoZhi Yang  <https://orcid.org/0000-0002-1859-4949>

## References

- Antoci, V., Cunha, M., Houdek, G., et al. 2014, *ApJ*, 796, 118  
 Baran, A. S., Koen, C., & Pokrzywka, B. 2015, *MNRAS*, 448, L16  
 Barac, N., Bedding, T. R., Murphy, S. J., et al. 2022, *MNRAS*, 516, 2080  
 Balona, L. A. 2014, *MNRAS*, 437, 1476  
 Balona, L. A., Baran, A. S., Daszyńska-Daszkiewicz, J., et al. 2015, *MNRAS*, 451, 1445  
 Balona, L. A. 2018, *MNRAS*, 479, 183  
 Balona, L. A. 2019, *MNRAS*, 490, 2112  
 Balona, L. A. 2021, *FrASS*, 8, 32  
 Bedding, T. R., Murphy, S. J., Hey, D. R., et al. 2020, *Natur*, 581, 147  
 Berthomieu, G., & Provost, J. 1983, *A&A*, 122, 199  
 Blazère, A., Petit, P., Lignières, F., et al. 2016, *A&A*, 586, A97  
 Böhm, T., Holschneider, M., Lignières, F., et al. 2015, *A&A*, 577, A64  
 Bouabid, M.-P., Montalbán, J., Miglio, A., et al. 2009, in *AIP Conf. Proc.* 1170, *Stellar Pulsation: Challenges for Theory and Observation* (College Park, MD: AIP), 477  
 Bouabid, M.-P., Dupret, M.-A., Salmon, S., et al. 2013, *MNRAS*, 429, 2500  
 Bouchaud, K., Domiciano de Souza, A., Rieutord, M., et al. 2020, *A&A*, 633, A78  
 Braithwaite, J., & Cantiello, M. 2013, *MNRAS*, 428, 2789  
 Brasseur, C. E., Phillip, C., Fleming, S. W., et al. 2019, *Astrocute: Tools for creating cutouts of TESS images*, *Astrophysics Source Code Library*, ascl:1905.007  
 Breger, M., Handler, G., Garrido, R., et al. 1999, *A&A*, 349, 225  
 Breger, M. 2000, in *ASP Conf. Ser.* 210, *Delta Scuti and Related Stars* (San Francisco, CA: ASP), 3  
 Breger, M., Fossati, L., Balona, L., et al. 2012, *ApJ*, 759, 62  
 Cantiello, M., & Braithwaite, J. 2019, *ApJ*, 883, 106  
 Chevalier, C. 1971, *A&A*, 14, 24  
 Davenport, J. R. A., Hebb, L., & Hawley, S. L. 2015, *ApJ*, 806, 212  
 Deheuvels, S., Ballot, J., Beck, P. G., et al. 2015, *A&A*, 580, A96  
 Dintrans, B., & Rieutord, M. 2000, *A&A*, 354, 86  
 Domiciano de Souza, A., Kervella, P., Jankov, S., et al. 2005, *A&A*, 442, 567  
 Dupret, M.-A., Grigahcène, A., Garrido, R., et al. 2006, *MmSAI*, 77, 366  
 Erspamer, D., & North, P. 2003, *A&A*, 398, 1121  
 Espinosa Lara, F., & Rieutord, M. 2013, *A&A*, 552, A35  
 García Hernández, A., Moya, A., Michel, E., et al. 2009, *A&A*, 506, 79  
 García Hernández, A., Moya, A., Michel, E., et al. 2013, *A&A*, 559, A63  
 García Hernández, A., Martín-Ruiz, S., Monteiro, M. J. P. F. G., et al. 2015, *ApJL*, 811, L29  
 García Hernández, A., Suárez, J. C., Moya, A., et al. 2017, *MNRAS*, 471, L140  
 Giles, H. A. C., Collier Cameron, A., & Haywood, R. D. 2017, *MNRAS*, 472, 1618  
 Gilliland, R. L., Brown, T. M., Christensen-Dalsgaard, J., et al. 2010, *PASP*, 122, 131  
 Goupil, M.-J., Dupret, M. A., Samadi, R., et al. 2005, *JApA*, 26, 249  
 Grigahcène, A., Dupret, M.-A., Gabriel, M., et al. 2005, *A&A*, 434, 1055  
 Grigahcène, A., Uytterhoeven, K., Antoci, V., et al. 2010, *AN*, 331, 989  
 Grigahcène, A., Antoci, V., Balona, L., et al. 2010, *ApJL*, 713, L192  
 Handler, G., & Breger, M. 1997, *DSSN*, 10, 11  
 Hasanzadeh, A., Safari, H., & Ghasemi, H. 2021, *MNRAS*, 505, 1476  
 Hey, D. R., Murphy, S. J., Foreman-Mackey, D., et al. 2020, *AJ*, 159, 202  
 Hey, D. R., Murphy, S. J., Foreman-Mackey, D., et al. 2022, *maelstrom: Forward modeling of pulsating stars in binaries*, *Astrophysics Source Code Library*, ascl:2205.005  
 Jenkins, J. M., Twicken, J. D., McCauliff, S., et al. 2016, *Proc. SPIE*, 9913, 99133E  
 Kaye, A. B., Handler, G., Krisciunas, K., et al. 1999, *PASP*, 111, 840  
 Kepler Mission Team 2009, *VizieR On-line Data Catalog*, V/133  
 Koch, D. G., Borucki, W. J., Basri, G., et al. 2010, *ApJL*, 713, L79  
 Kurtz, D. W. 1985, *MNRAS*, 213, 773  
 Kurtz, D. W., Saio, H., Takata, M., et al. 2014, *MNRAS*, 444, 102  
 Lenz, P., & Breger, M. 2005, *CoAst*, 146, 53  
 Le Dizès, C., Rieutord, M., & Charpinet, S. 2021, *A&A*, 653, A26  
 Li, G., Van Reeth, T., Bedding, T. R., et al. 2019, *MNRAS*, 487, 782  
 Li, G., Van Reeth, T., Bedding, T. R., et al. 2020, *MNRAS*, 491, 3586  
 Lignières, F., Rieutord, M., & Reese, D. 2006, *A&A*, 455, 607  
 Lignières, F., & Georgeot, B. 2009, *A&A*, 500, 1173  
 Lightkurve Collaboration, Cardoso, J. V. de M., Hedges, C., et al. 2018, *Lightkurve: Kepler and TESS time series analysis in Python*, *Astrophysics Source Code Library*, ascl:1812.013  
 Lignières, F., & Georgeot, B. 2008, *PhRvE*, 78, 016215  
 Maeder, A., & Meynet, G. 2004, *A&A*, 422, 225  
 Maeder, A. 2009, *Physics, Formation and Evolution of Rotating Stars: Astronomy and Astrophysics Library* (Berlin: Springer), 2009  
 Mirouh, G. M., Reese, D. R., Faure, G., et al. 2021, in *MOBSTER-1 virtual conference: Stellar Variability as a Probe of Magnetic Fields in Massive Stars*, doi:10.5281/zenodo.5563045  
 Molnár, L., Bódi, A., Pál, A., et al. 2022, *ApJS*, 258, 8  
 Monnier, J. D., Zhao, M., Pedretti, E., et al. 2007, *Sci*, 317, 342  
 Montgomery, M. H., & O'Donoghue, D. 1999, *DSSN*, 13, 28  
 Moya, A., Zuccarino, F., Chaplin, W. J., et al. 2018, *ApJS*, 237, 21  
 Moya, A., & López-Sastre, R. J. 2022, *A&A*, 663, A112  
 Murphy, S. J. 2012, *MNRAS*, 422, 665  
 Murphy, S. J., Bedding, T. R., Shibahashi, H., et al. 2014, *MNRAS*, 441, 2515  
 Murphy, S. J., & Shibahashi, H. 2015, *MNRAS*, 450, 4475

- Murphy, S. J., Shibahashi, H., & Bedding, T. R. 2016, *MNRAS*, 461, 4215
- Murphy, S. J., Moe, M., Kurtz, D. W., et al. 2018, *MNRAS*, 474, 4322
- Murphy, S. J., Saio, H., Takada-Hidai, M., et al. 2020, *MNRAS*, 498, 4272
- Nielsen, M. B., Gizon, L., Schunker, H., et al. 2013, *A&A*, 557, L10
- Ouazzani, R.-M., Roxburgh, I. W., & Dupret, M.-A. 2015, *A&A*, 579, A116
- Ouazzani, R.-M., Salmon, S. J. A. J., Antoci, V., et al. 2017, *MNRAS*, 465, 2294
- Paparo, M., Benkó, J. M., Hareter, M., et al. 2016, *ApJS*, 224, 41
- Paxton, B., Smolec, R., Schwab, J., et al. 2019, *ApJS*, 243, 10
- Petit, P., Lignières, F., Wade, G. A., et al. 2010, *A&A*, 523, A41
- Ramón-Ballesta, A., García Hernández, A., Suárez, J. C., et al. 2021, *MNRAS*, 505, 6217
- Reese, D., Lignières, F., & Rieutord, M. 2006, *A&A*, 455, 621
- Reese, D., Lignières, F., & Rieutord, M. 2008, *A&A*, 481, 449
- Reese, D. R., Lignières, F., Ballot, J., et al. 2017a, *A&A*, 601, A130
- Reese, D. R., Dupret, M.-A., & Rieutord, M. 2017b, *EPJWC*, 160, 02007
- Reese, D. R., Mirouh, G. M., Espinosa Lara, F., et al. 2021, *A&A*, 645, A46
- Reiners, A., & Royer, F. 2004, *A&A*, 428, 199
- Ricker, G. R., Winn, J. N., Vanderspek, R., et al. 2015, *JATIS*, 1, 014003
- Rieutord, M., Espinosa Lara, F., & Putigny, B. 2016, *JCoPh*, 318, 277
- Rieutord, M., & Valdettaro, L. 2018, *JFM*, 844, 597
- Royer, F., Grenier, S., Baylac, M.-O., et al. 2002, *A&A*, 393, 897
- Royer, F., Zorec, J., & Gómez, A. E. 2007, *A&A*, 463, 671
- Saio, H., Kurtz, D. W., Takata, M., et al. 2015, *MNRAS*, 447, 3264
- Saio, H., Kurtz, D. W., Murphy, S. J., et al. 2018a, *MNRAS*, 474, 2774
- Saio, H., Bedding, T. R., Kurtz, D. W., et al. 2018b, *MNRAS*, 477, 2183
- Sánchez Arias, J. P., Romero, A. D., Córscico, A. H., et al. 2018, *A&A*, 616, A80
- Samadi-Ghadim, A., Lampens, P., Jassur, D. M., et al. 2020, *A&A*, 638, A57
- Savanov, I. S. 2019, in ASP Conf. Ser. 518, Physics of Magnetic Stars (San Francisco, CA: ASP), 195
- Stassun, K. G., Oelkers, R. J., Paegert, M., et al. 2019, *AJ*, 158, 138
- Stello, D., Saunders, N., Grunblatt, S., et al. 2022, *MNRAS*, 512, 1677
- Stellingwerf, R. F. 1979, *ApJ*, 227, 935
- Stumpe, M. C., Smith, J. C., Catanzarite, J. H., et al. 2014, *PASP*, 126, 100
- Suárez, J. C., Bruntt, H., & Buzasi, D. 2005, *A&A*, 438, 633
- Suárez, J. C., García Hernández, A., Moya, A., et al. 2014, *A&A*, 563, A7
- Uytterhoeven, K., Moya, A., Grigahcène, A., et al. 2011, *A&A*, 534, A125
- van Belle, G. T., Ciardi, D. R., Thompson, R. R., et al. 2001, *ApJ*, 559, 1155
- van Leeuwen, F. 2007, *A&A*, 474, 653
- Van Reeth, T., Tkachenko, A., & Aerts, C. 2016, *A&A*, 593, A120
- Xiang, M., Rix, H.-W., Ting, Y.-S., et al. 2022, *A&A*, 662, A66
- Xiong, D. R., Deng, L., Zhang, C., et al. 2016, *MNRAS*, 457, 3163
- Yang, T., Esamdin, A., Song, F., et al. 2018, *ApJ*, 863, 195
- Zorec, J., & Royer, F. 2012, *A&A*, 537, A120